Record-large magnetically driven polarization in room temperature ferromagnets OsX_2 monolayers

Ying Zhou,[1] Haoshen Ye,[1] Junting Zhang [●],[2] and Shuai Dong [●][1,*]

[1]*Key Laboratory of Quantum Materials and Devices of Ministry of Education, School of Physics, Southeast University, Nanjing 211189, China*
[2]*School of Materials Science and Physics, China University of Mining and Technology, Xuzhou 221116, China*

Magnetically induced ferroelectrics in multiferroics provide an optimal approach to the pursuit of intrinsically strong magnetoelectricity. However, the complex antiferromagnetism, faint magnetically induced polarization, and low working temperatures make their magnetoelectric performance incompetent from the application's demands. Here, a family of two-dimensional $5d$ halides OsX_2 monolayers is predicted to be ferroelectric and ferromagnetic above room temperature. More interestingly, benefiting from the strong spin-orbital coupling and high-spin state of Os^{2+} ion, the magnetically induced ferroelectric polarization can reach 5.9 μC/cm^2, a record-large value in type-II multiferroics. The magnetoelectric effect, that is, controlling ferroelectric polarization by magnetic field has been demonstrated, and magnetically driven ferrovalley also emerges in this system. This work provides an effective way to solve the main defects of type-II multiferroics.

I. INTRODUCTION

With the increasing demands for high-performance electronic devices, multiferroic materials with more than one ferroic order have attracted much attention [1–6]. The intrinsic coupling between/among these ferroic orders can lead to cross manipulations, which can be employed in various applications [7,8]. Depending on the origin of ferroelectricity, multiferroics can be categorized into the type-I and type-II ones [9]. The type-I multiferroics with independent origins of magnetism and ferroelectricity are believed to be naturally weak regarding the intrinsic magnetoelectricity, even if their ferroelectricity and/or magnetism may be prominent [10]. In contrast, the type-II multiferroics with polarization generated by particular magnetism were highly desired for their intrinsic strong magnetoelectricity [11–13].

However, despite the great progress in the past decades, there remain some serious and inevitable drawbacks for type-II multiferroics, which hinder their further development. First, the magnetically induced ferroelectric polarization is very weak compared with that of conventional proper ferroelectrics ($10 - 100$ μC/cm^2) [10,14,15]. For example, for typical type-II multiferroics with spiral spin order, their polarization is 0.016 μC/cm^2 and 0.08 μC/cm^2 for CuO and TbMnO$_3$ [11,16], respectively. Relative larger polarization is derived from the nonrelativistic exchange-striction mechanism, which leads to 0.12 μC/cm^2 and 0.8 μC/cm^2 in the GdFeO$_3$ and o-YMnO$_3$ [12,17], respectively. Second, most type-II multiferroics are antiferromagnets with complex spin textures (e.g., noncollinear/nonplanar, staggered/zigzag) originating from magnetic frustrations, which not only reduces the ordering temperatures but also leads to weak responses to external magnetic fields [18–20].

In another branch (the so-called linear magnetoelectricity), the magnetically induced polarization is linearly proportional to the magnetic field. However, the magnetically induced polarization is also typically faint because the underlying mechanisms are similar to those of type-II multiferroics [4]. Even for the so-called colossal linear magnetoelectricity in Fe$_2$Mo$_3$O$_8$, its magnetically induced polarization is only ~ 0.6 μC/cm^2 [21].

The $5d$ electron systems may be the solution to resolve this long-term predicament [22]. The spin-orbital coupling (SOC), which usually plays as the glue between magnetism and polarity [4], is much larger in $5d$ electron systems. In addition, the broad spatial extension of $5d$ electron cloud is helpful to enhance the orbital overlaps and thus the exchange interactions, a key factor to improving the working temperature. Despite these positive factors, the known $5d$ multiferroics remain rare due to the following reasons. Their weak Hund coupling often fails when competing with the crystal field, resulting in a low spin state for $5d$ ions, which is disadvantageous to stabilize a local magnetic moment. In addition, the broad extension of $5d$ orbitals leads to a large bandwidth, which tends to overcome the weak Hubbard U and result in a metallic state.

Therefore, to pursue type-II multiferroics containing $5d$ ions, the delicate balance among multiple interactions should be carefully tuned. First, the crystal field splitting should be minimized to obtain the high spin state. Compared with divalent O^{2-} and trivalent N^{3-}, the halogen X^- is less charged, which can systematically reduce the crystal field [23]. Thus, halides are preferred over oxides and nitrides. Second, the bandwidth of $5d$ orbitals should be moderate to avoid metallicity. Two-dimensional (2D) van der Waals materials may be proper candidates, in which the quantum confinement effect can narrow the bandwidth and increase the band gap to a certain extent. For 2D metal halides, there are two common families MX_2 and MX_3 monolayers, which form the triangular prism and octahedral coordination, respectively. As shown
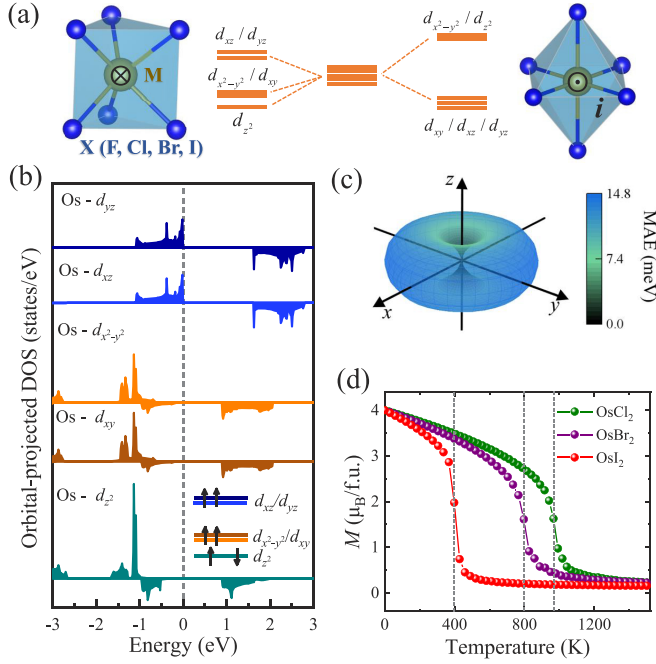

FIG. 1. (a) Schematic of the prism-type and octahedral crystalline field splittings of d orbitals. The $\otimes$ and $\odot$ on magnetic ions represent the breaking and preservation of the inversion center (i), respectively. (b) The orbital-projected density of states (DOS) of $OsCl_2$ monolayer. (c) The polar plot of MAE. (d) The MC simulations for ferromagnetic transitions of OsX_2 monolayers.

in Fig. 1(a), the former has relatively smaller splitting gaps. More importantly, the octahedral coordination preserves the inversion center, thus ruling out the possibility of magnetically induced ferroelectricity in ferromagnets. Therefore, the MX_2 monolayer systems are promising candidates for type-II multiferroics with excellent magnetoelectricity.

In this paper, following the above design principles, we predict OsX_2 monolayers as $5d$ type-II multiferroics with prominent performance by using first-principles calculations. Our results show that in this system, magnetically induced ferroelectricity and ferromagnetism are compatible and coupled, with Curie temperature above room temperature. The dependence of the induced polarization on the spin direction can be explained by the $p - d$ hybridization mechanism involving SOC. The strong SOC of Os ions leads to a large polarization of 5.9 $\mu C/cm^2$, the largest value among known type-II multiferroic materials. Besides ferroelectricity and ferromagnetism, magnetically driven ferrovalley also emerges and can be controlled by a magnetic field.

II. COMPUTATIONAL METHODS

The first-principles calculations based on density functional theory (DFT) were performed using the projector-augmented wave method, as implemented in the Vienna *ab initio* Simulation Package [24–26]. The Perdew-Burke-Ernzerhof functional was used as the exchange-correlation functional [27,28]. A vacuum space of 20 Å was added to avoid interaction between neighboring periodic images. We used a cutoff energy of 600 eV for the plane-wave bases

and a Γ-centered $15 \times 15 \times 1$ k-point mesh for the Brillouin zone integration. The in-plane lattice constants and internal atomic coordinates of each structural phase were relaxed until the Hellman-Feynman force on each atom was less than 0.005 eV/Å. A convergence threshold of 10^{-7} eV was used for the electronic self-consistency loop.

To describe correlated $5d$ electrons of Os, the GGA + U method is applied [29], and the U_{eff} is tested from 0 to 2 eV [see Supplementary Material (SM) for more details [30]]. For comparison, the Heyd-Scuseria-Ernzerhof (HSE06) hybrid functional was also considered [31]. Since the band structure at $U_{eff} = 1.5$ eV is the most consistent one with that obtained from the HSE06 hybrid functional, $U_{eff} = 1.5$ eV will be adopted as default in the following discussion.

Phonon band structures were calculated using density functional perturbation theory (DFPT). The phonon frequencies and corresponding eigenmodes were calculated on the basis of the extracted force-constant matrices with a $4 \times 4 \times 1$ supercell, as implemented in the PHONOPY code [32]. The ferroelectric polarization was calculated by using the Berry phase method [33].

In addition, Monte Carlo (MC) simulations were performed to verify the magnetic ground states and estimate the magnetic transition temperatures. The T_C is estimated via the Monte Carlo simulation on the classical spin model, which can be written as

$$H = -\sum_{\langle i,j \rangle} J_{ij} \mathbf{S}_i \cdot \mathbf{S}_j - A \sum_i \left(\mathbf{S}_i^z \right)^2, \qquad (1)$$

with J and A as the exchange parameters and the anisotropy constant, respectively. The nearest neighboring J_1, next-nearest neighboring J_2, and third-nearest neighboring J_3 are considered, which can be extracted from the DFT energies. A 30×30 triangular lattice is used in our MC simulation. MC steps for both thermal equilibrium and measurement sampling by the Metropolis algorithm are 10 000 steps.

III. RESULTS AND DISCUSSION

A. Crystal structure and magnetism

Figure 1(a) illustrates the crystal structure of OsX_2 ($X =$ F, Cl, Br, and I) monolayers with space group $P\bar{6}m2$ (the 2H-phase of MX_2), which is nonpolar and noncentrosymmetric. As shown in Fig. S1 in the SM [30], there are no imaginary modes in phonon dispersions of all OsX_2 except OsF_2, indicating dynamic stability of OsX_2 ($X =$ Cl, Br, and I). This provides a solid guide for successful experimental fabrication. Like other 2D ferromagnetic materials such as VSe_2 [34,35] and CrI_3 [36], OsX_2 might be grown using methods like chemical vapor deposition (CVD) or chemical vapor transport (CVT), followed by mechanical exfoliation down to monolayers. Subsequently, characterization techniques such as atomic force microscopy (AFM), scanning electron microscopy (SEM), and x-ray photoelectron spectroscopy (XPS) are employed to analyze their structure and properties. As these three monolayers share similar properties, we only focus on monolayer $OsCl_2$ as a representative in the following.

The optimized lattice constant of the $OsCl_2$ monolayer is 3.43 Å. For every Os^{2+} ion, the six unpaired electrons occupy the $5d$ orbitals and form the high spin state, i.e., five spin-up

TABLE I. Ferromagnetic, ferroelectric, and ferrovalley properties of OsX_2 monolayers with $U_{eff} = 1.5\,eV$. The MAE (A), exchange coefficients (J's), magnetic moment (M), band gap, and the maximum in-plane and out-of-plane polarization (P_x^{max}, P_z^{max}) are presented. J_1, J_2, and J_3 denote the nearest-neighbor, next-nearest-neighbor, and third-nearest-neighbor exchange interactions, respectively. To calculate the polarization, the thickness of monolayers is used to estimate the volumes.

Materials	$OsCl_2$	$OsBr_2$	OsI_2
A (meV/f.u.)	14.8	16.5	30.0
J_1 (meV/f.u.)	77.1	56.8	35.4
J_2 (meV/f.u.)	10.0	3.1	−0.1
J_3 (meV/f.u.)	−12.0	−3.8	−6.7
T_C (K)	966	796	398
M (μ_B/Os)	4.0	4.0	4.0
Band gap (meV)	470	415	21
P_x^{max} ($\mu C/cm^2$)	2.5	2.6	5.9
P_z^{max} (nC/cm^2)	6.9	15.5	31.2
ΔE_K^{VBM} (meV)	128	77	47

and one spin-down mainly in the $3z^2 - r^2$ orbital, as shown in Fig. 1(b). Such a high spin state can only be stabilized when the crystal field splitting is weak between the xz/yz and $x^2 - y^2/xy$ orbitals. Consequently, the Os^{2+} exhibits a large magnetic moment $4\,\mu_B$, which is confirmed in our DFT calculation. The magnetocrystalline anisotropy energy (MAE) is calculated with SOC enabled as the energy difference between different spin directions. Our result indicates an easy magnetic axis along the out-of-plane direction for the $OsCl_2$ monolayer, as shown in Fig. 1(c). Due to the strong SOC, its MAE is rather large, reaching 14.8 meV/Os.

Furthermore, by comparing the ferromagnetic and three most possible antiferromagnetic configurations (as shown in Fig. S2 in the SM [30]), the ferromagnetic state is found to be the most energetically stable, as summarized in Table S1 in the SM [30]. Using the normalized spin $|S| = 1$, the nearest-neighbor exchange J_1 is estimated as 77.1 meV, a quite strong ferromagnetic coupling, while the second- and third-neighbor ones are relatively weaker ($J_2 = 10.0$ meV and $J_3 = -12.0$ meV). The ferromagnetic Curie temperature T_C of $OsCl_2$ monolayer is then predicted to be ~966 K via an MC simulation of the class spin model, as shown in Fig. 1(d).

The magnetic properties of $OsBr_2$ and OsI_2 are also calculated, as compared in Table I. Both of them are ferromagnetic with a common magnetic easy axis pointing out of plane (i.e. z axis). It can be found that the J_1 and the associated T_C are much larger/higher in $OsCl_2$ than in the other two. The physical reason is the much shorter Os-Cl bond (2.61 Å) than the others (2.74 Å for Os-Br and 2.91 Å for Os-I) due to the smallest size and strongest electronegativity of the Cl^- ion, which strengthens the $p - d$ orbital hybridization. However, the estimated T_C of $OsBr_2$ and OsI_2 remain above room temperature. It is mainly due to the large ferromagnetic J_1, which is naturally superior of $5d$ magnets, inherited from its more spatial expansion of electronic clouds. In addition, the MAE increases with an atomic number of X, as expected from the increasing SOC.
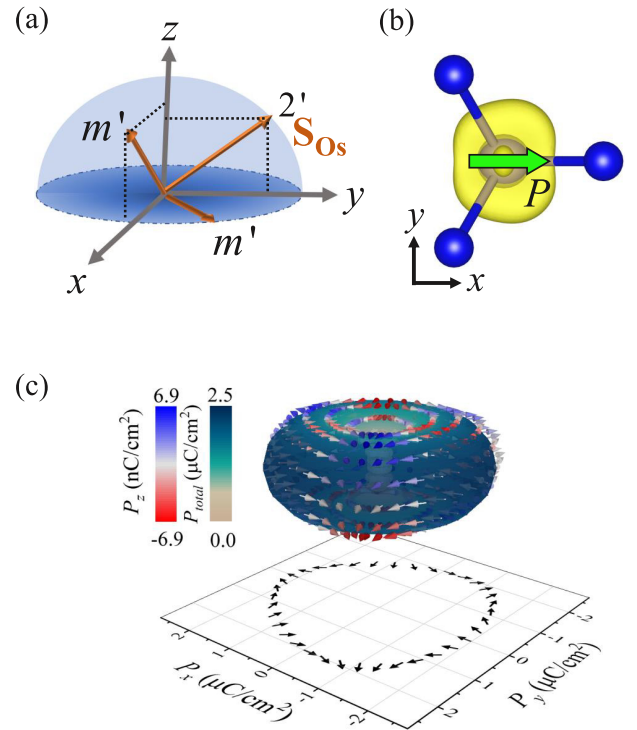

FIG. 2. (a) The evolution of MPG as the spin rotates within the xy plane, xz plane, and yz plane. The orange arrow denotes the spin of Os (S_{Os}). Here, x axis and z axis are the in-plane two-fold rotation axis and the out-of-plane three-fold rotation axis, respectively. The xz plane and xy plane are vertical mirror plane and horizontal mirror plane, respectively. The m' within the xz plane preserves the vertical mirror plane, while the m' within the xy plane preserves the horizontal mirror plane. (b) Differential electron density between the states with spin along the x axis and z axis. (c) Three-dimensional polar plot of polarization for $OsCl_2$. The projection to the xy plane is also shown. For better stereoscopic view, the value of P_z component is magnified 300 times.

For completeness, the magnetism of OsX_2 are tested as a function of U_{eff} from 0 to 2 eV, as summarized in Tables S1–S4 in the SM [30]. For the $OsCl_2$ and $OsBr_2$, the MAE monotonically decreases as U_{eff} increases from 0 to 2 eV. It can be understood from second-order perturbation theory analysis [37], which is related to the valence and conduction bands moving farther away from the Fermi level as U_{eff} increases, as shown in Fig. S3 in the SM [30]. For most U_{eff}, there are no qualitative differences, except for $U_{eff} = 0$ eV for OsI_2.

B. Ferroelectricity

We next investigated the ferroelectricity of the OsX_2 monolayers. The magnetic point group (MPG) for this ground state (out-of-plane magnetocrystalline anisotropy) is $\bar{6}m'2'$, which is nonpolar. Polarization can be induced when spin rotates away from the z axis, as shown in Fig. 2(a). For spin along an arbitrary direction in the xz plane (except the x and z axes), the in-plane two-fold rotation symmetry and horizontal mirror symmetry are broken, and thus the MPG becomes m', as shown in Fig. 2(a). Thus, both the in-plane and

out-of-plane components of polarization (i.e., P_x and P_z, and $P_y = 0$) are allowed. The corresponding polar plots of P_x and P_z are shown in Fig. S4(b) in the SM [30]. The numerical values obtained via DFT calculation agree with the analytic formula very well. The maximum value of the in-plane polarization component reaches 2.5 $\mu C/cm^2$ for the $OsCl_2$ monolayer, while the value of the out-of-plane polarization component is only 6.9 nC/cm^2.

This magnetically induced polarization can be visualized using the differential electron density between the two states: spin along the x and z axis, as shown in Fig. 2(b). The in-plane charge distribution along the ligand directions is not uniform, leading to the appearance of in-plane polarization.

For spin along an arbitrary direction in the yz plane (except the y and z axes), the horizontal and vertical mirror symmetries are broken, and thus the MPG becomes $2'$, and only the in-plane P_x component of polarization is allowed. The corresponding polar plot of P_x is shown in Fig. S4(c) in the SM [30]. For spin along other arbitrary directions (except in the $xy/xz/yz$ planes), all symmetries are broken, and MPG becomes 1. Then, all components of polarization are allowed. A three-dimensional polar plot (and its projection to the xy plane) of **P** obtained in a DFT calculation is shown Fig. 2(c), which forms a horn torus.

The origin of polarization can be explained by the $p - d$ hybrid mechanism, which is related to the SOC effect [38]. It can be obtained by summing the charge transfers between the magnetic ion and its ligands, expressed as $\mathbf{P} \propto \sum_i^n (\mathbf{S} \cdot \mathbf{e}_i)^2 \cdot \mathbf{e}_i$, where $\mathbf{e}_i$ is the unit vector of the bond between the magnetic ion and ligands, and **S** is the vector of spin. Therefore, the net **P** of OsX_2 monolayers can be expressed as

$$\mathbf{P} = (P_x, P_y, P_z) \propto (S_x^2 - S_y^2, -2S_xS_y, 0), \qquad (2)$$

which can also describe the magnetically induced polarization in other 2H-type ferromagnetic monolayers such as VSe_2, VTe_2, and $RuBr_2$ [39,40]. However, Eq. 2 can only explain the major in-plane polarization, while the tiny P_z obtained in a DFT calculation must come from the high-order terms of the SOC effect [39,41]. The out-of-plane polarization becomes

$$P_z \propto (4S_x^3S_z + 4\sqrt{3}S_x^2S_yS_z + 12S_xS_y^2S_z). \qquad (3)$$

Since here the magnetically induced polarization is generated via a SOC process, the intensity of SOC plays a key role in the magnitude of polarization. It is the reason that $OsCl_2$ owns a much larger polarization than VSe_2 [39] due to the strong SOC of $5d$ orbitals. Furthermore, the polarization of $OsBr_2$ and OsI_2 can be even larger due to the additional large SOC from anions, as compared in Table I. The largest polarization reaches ∼5.9 $\mu C/cm^2$ in OsI_2 monolayer ($U_{eff} = 1.5$ eV), a record-large value in magnetically induced polarization and even comparable to the magnitude of geometric ferroelectrics [42]. Meanwhile, the P_z is also enhanced by larger SOC from anions, as shown in Table I.

The strong coupling between spin and polarization makes a magnetic field an effective strategy for manipulating the polarization of OsX_2 monolayers. By considering the MAE and Zeeman energy, a model Hamiltonian can be expressed as

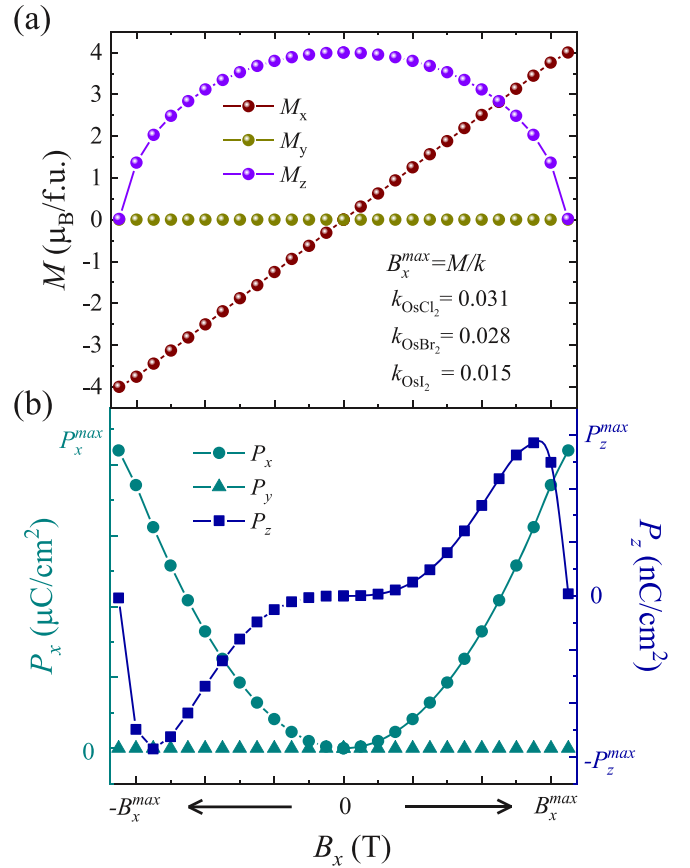$$E = E_{MAE} + E_{B_x} = A \sin^2\theta - M \sin\theta B_x, \qquad (4)$$

FIG. 3. Magnetic field tuning of magnetoelectric properties of OsX_2 monolayers at zero temperature. The magnetic field is applied along the x axis. (a) Three components of magnetization. The x component of magnetization is proportional to the field linearly. (b) Three components of polarization components. The x component of polarization is in a parabolic function of the field. B_x^{max} is the field required for magnetizatic saturation.

in which B_x denotes the external magnetic field along the x-axis, M is the magnetization $4 \mu_B/Os$, and θ is the polar angle. The equilibrium state can be obtained by $\partial E/\partial \theta = 0$. It is then straightforward to obtain the relationship between the in-plane component of magnetization (M_x) and B_x as

$$M_x = 2MB_x/A, \qquad (5)$$

which is a linear function with a slope coefficient $k = 2M/A$ before the saturation, as shown in Fig. 3(a).

Meanwhile, the magnetically induced in-plane polarization $P_x \propto S_x^2 \propto M_x^2$. Therefore, $P_x \propto B_x^2$ [Fig. 3(b)], a parabolic behavior different from the well-known linear magnetoelectricity.

C. Ferrovalley

In addition to ferromagnetism and ferroelectricity, OsX_2 monolayers can also exhibit the ferrovalley degree of freedom. Figure 4 shows their band structures at $U_{eff} = 1.5$ eV. The VBM are different at the K_+ and K_- points when spin points along the z axis, as shown in the left panels of Fig. 4. Here, the valley polarization is defined as $\Delta E_K = E_{K_+} - E_{K_-}$, where E_{K_+} and E_{K_-} refer to the energies of valence band maximum
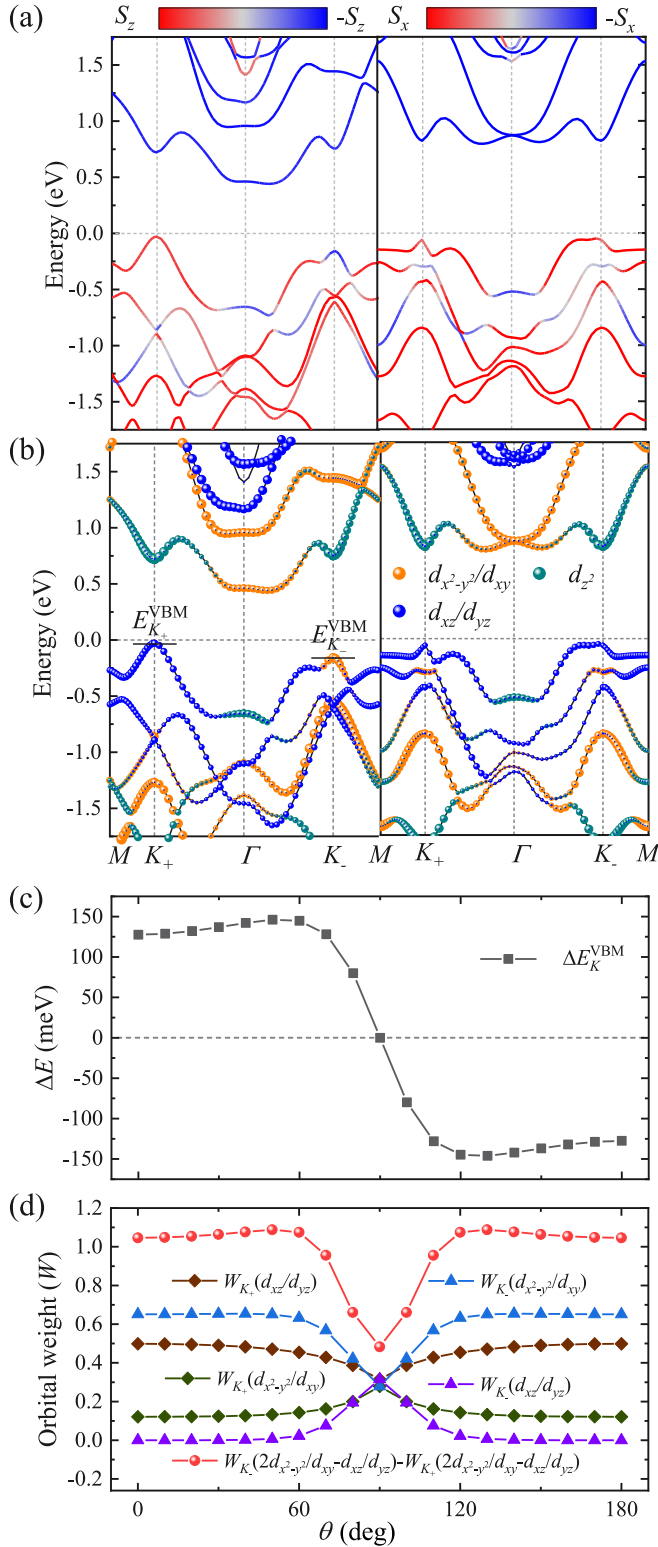
FIG. 4. Ferrovalley of $OsCl_2$ monolayer. (a) Spin-projected band structures and (b) Orbital-projected band structures obtained at $U_{eff} = 1.5$ eV. Left panels: spin points along z axis; Right panels: spin points along x axis. (c) The magnitude of valley splitting of the VBM at the $K_{+/-}$ points as a function of the spin polar angle. (d) The orbital weights of the VBM at the $K_{+/-}$ points as a function of the spin polar angle.

(VBM) at the K_+ and K_- points, respectively. For $OsCl_2$ monolayer, ΔE_K^{VBM} reaches 128 meV. This valley polarization disappears when spin lies in the xy plane as shown in the right panels of Fig. 4. The valley polarization of $OsBr_2$ and OsI_2 monolayers are summarized in Table I.

Although the ferrovalley properties generally exist in many monolayers, here $OsCl_2$ exhibits some unique phenomena. In other ferrovalley materials such as VSe_2 and $RuCl_2$, neither the spin nor the orbital projection of the VBM undergoes a significant change when the valley polarization is switched [43–45]. In contrast, here in the ferrovalley state with spin pointing along the z axis, the dominant spin component of VBM at the K_- valley is reversed [Fig. 4(a)], and the dominant orbital component of VBM is also changed at the K_- valley [Fig. 4(b)].

Such significant spin-orbital reconstruction of the valley state is a consequence of strong SOC of Os ion [46,47], which will lead to the nontrivial tuning of ferrovalley polarization. Figure 4(c) shows ΔE_K's of VBM as a function of spin polar angle θ. The VBM curve is anomalous, which reaches the maximum value when θ is 60° or 120°. For comparison, the largest valley polarization always appears when spin points along the z axis in VSe_2 [39], VSi_2N_4 [43], and Nb_3I_8 [45].

The orbital weights (W's) of the VBM obtained in the DFT calculations may provide an explanation for the aforementioned phenomenon. As shown in Fig. 4(d), when spin points along the z axis ($\theta = 0°$), the K_- valley is primarily contributed by the $d_{x^2-y^2}/d_{xy}$ orbitals, while the K_+ valley is primarily contributed by the d_{xz}/d_{yz}. When the spin points along the x axis ($\theta = 90°$), the contributions from the d_{xz}/d_{yz} orbitals and $d_{x^2-y^2}/d_{xy}$ orbitals are almost equal to the VBMs of both K_+ and K_- valleys. Interestingly, the sum of orbital weights differences of K_+ and K_- also exhibits the maximum value when θ is 60° or 120°.

IV. CONCLUSION

In summary, our work has demonstrated that OsX_2 monolayers are candidates for low-dimensional functional materials exhibiting excellent ferromagnetic, ferroelectric, and ferrovalley properties, as well as magnetoelectric and magneto-valley coupling effects. In particular, OsX_2 monolayers own high ferromagnetic Curie temperatures above room temperature and their magnetically induced polarization can reach several $\mu C/cm^2$. A parabolic magnetoelectric behavior is predicted, distinguishing them from those with linear magnetoelectricity. Furthermore, the ferromagnetic ground state protects the intrinsic valley polarization.

[1] C. Gong, L. Li, Z. Li, H. Ji, A. Stern, Y. Xia, T. Cao, W. Bao, C. Wang, Y. Wang, Z. Q. Qiu, R. J. Cava, S. G. Louie, J. Xia, and X. Zhang, Discovery of intrinsic ferromagnetism in two-dimensional van der Waals crystals, Nature (London) **546**, 265 (2017).

[2] L. Li and M. Wu, Binary compound bilayer and multilayer with vertical polarizations: Two-dimensional ferroelectrics, multiferroics, and nanogenerators, ACS Nano **11**, 6382 (2017).

[3] S. Dong, J.-M. Liu, S.-W. Cheong, and Z. Ren, Multiferroic materials and magnetoelectric physics: Symmetry, entanglement, excitation, and topology, Adv. Phys. **64**, 519 (2015).

[4] S. Dong, H. Xiang, and E. Dagotto, Magnetoelectricity in multiferroics: a theoretical perspective, Natl. Sci. Rev. **6**, 629 (2019).

[5] N. A. Spaldin and R. Ramesh, Advances in magnetoelectric multiferroics, Nat. Mater. **18**, 203 (2019).

[6] N. A. Spaldin, Multiferroics: Past, present, and future, MRS Bull. **42**, 385 (2017).

[7] D. Zhong, K. L. Seyler, X. Linpeng, R. Cheng, N. Sivadas, B. Huang, E. Schmidgall, T. Taniguchi, K. Watanabe, M. A. McGuire, W. Yao, D. Xiao, K.-M. C. Fu, and X. Xu, Van der Waals engineering of ferromagnetic semiconductor heterostructures for spin and valleytronics, Sci. Adv. **3**, e1603113 (2017).

[8] A. Manchon, H. C. Koo, J. Nitta, S. M. Frolov, and R. A. Duine, New perspectives for Rashba spin-orbit coupling, Nat. Mater. **14**, 871 (2015).

[9] D. Khomskii, Classifying multiferroics: Mechanisms and effects, Physics **2**, 20 (2009).

[10] J. Wang, J. Neaton, H. Zheng, V. Nagarajan, S. Ogale, B. Liu, D. Viehland, V. Vaithyanathan, D. Schlom, U. Waghmare, N. Spaldin, K. Rabe, M. Wuttig, and R. Ramesh, Epitaxial BiFeO$_3$ multiferroic thin film heterostructures, Science **299**, 1719 (2003).

[11] T. Kimura, Y. Sekio, H. Nakamura, T. Siegrist, and A. P. Ramirez, Cupric oxide as an induced-multiferroic with high-T_C, Nat. Mater. **7**, 291 (2008).

[12] Y. Tokunaga, N. Furukawa, H. Sakai, Y. Taguchi, T.-h. Arima, and Y. Tokura, Composite domain walls in a multiferroic perovskite ferrite, Nat. Mater. **8**, 558 (2009).

[13] J. Zhang, Y. Zhou, F. Wang, X. Shen, J. Wang, and X. Lu, Coexistence and coupling of spin-induced ferroelectricity and ferromagnetism in perovskites, Phys. Rev. Lett. **129**, 117603 (2022).

[14] Y. K. Jeong, J.-H. Lee, S.-J. Ahn, S.-W. Song, H. M. Jang, H. Choi, and J. F. Scott, Structurally tailored hexagonal ferroelectricity and multiferroism in epitaxial YbFeO$_3$ thin-film heterostructures, J. Am. Chem. Soc. **134**, 1450 (2012).

[15] B. Van Aken, T. Palstra, A. Filippetti, and N. Spaldin, The origin of ferroelectricity in magnetoelectric YMnO$_3$, Nat. Mater. **3**, 164 (2004).

[16] T. Kimura, T. Goto, H. Shintani, K. Ishizaka, T. Arima, and Y. Tokura, Magnetic control of ferroelectric polarization, Nature (London) **426**, 55 (2003).

[17] M. Nakamura, Y. Tokunaga, M. Kawasaki, and Y. Tokura, Multiferroicity in an orthorhombic YMnO$_3$ single-crystal film, Appl. Phys. Lett. **98**, 082902 (2011).

[18] J.-J. Zhang, L. Lin, Y. Zhang, M. Wu, B. I. Yakobson, and S. Dong, Type-II multiferroic Hf$_2$VC$_2$F$_2$ MXene monolayer with high transition temperature, J. Am. Chem. Soc. **140**, 9768 (2018).

[19] C. Gong, E. M. Kim, Y. Wang, G. Lee, and X. Zhang, Multiferroicity in atomic van der Waals heterostructures, Nat. Commun. **10**, 2657 (2019).

[20] Q. Song, C. A. Occhialini, E. Ergecen, B. Ilyas, D. Amoroso, P. Barone, J. Kapeghian, K. Watanabe, T. Taniguchi, A. S. Botana, S. Picozzi, N. Gedik, and R. Comin, Evidence for a single-layer van der Waals multiferroic, Nature (London) **602**, 601 (2022).

[21] Y. Chang, Y. Weng, Y. Xie, B. You, J. Wang, L. Li, J.-M. Liu, S. Dong, and C. Lu, Colossal linear magnetoelectricity in polar magnet Fe$_2$Mo$_3$O$_8$, Phys. Rev. Lett. **131**, 136701 (2023).

[22] D. Hu, H. Ye, N. Ding, K. Xu, S.-S. Wang, S. Dong, and X. Yao, Two-dimensional 5d multiferroic W$_3$Cl$_8$: Breathing kagome lattice and tunable magneto-optical Kerr effect, Phys. Rev. B **109**, 014433 (2024).

[23] M. An and S. Dong, Ferroic orders in two-dimensional transition/rare-earth metal halides, APL Mater. **8**, 110704 (2020).

[24] G. Kresse and J. Furthmüller, Efficient iterative schemes for *ab initio* total-energy calculations using a plane-wave basis set, Phys. Rev. B **54**, 11169 (1996).

[25] G. Kresse and J. Furthmüller, Efficiency of ab-initio total energy calculations for metals and semiconductors using a plane-wave basis set, Comput. Mater. Sci. **6**, 15 (1996).

[26] P. E. Blöchl, Projector augmented-wave method, Phys. Rev. B **50**, 17953 (1994).

[27] G. Kresse and D. Joubert, From ultrasoft pseudopotentials to the projector augmented-wave method, Phys. Rev. B **59**, 1758 (1999).

[28] Y. Wang and J. P. Perdew, Correlation hole of the spin-polarized electron-gas, with exact small-wave-vector and high-density scaling, Phys. Rev. B **44**, 13298 (1991).

[29] S. L. Dudarev, G. A. Botton, S. Y. Savrasov, C. J. Humphreys, and A. P. Sutton, Electron-energy-loss spectra and the structural stability of nickel oxide: An LSDA+U study, Phys. Rev. B **57**, 1505 (1998).

[30] See Supplemental Material at http://link.aps.org/supplemental/10.1103/PhysRevMaterials.8.104403 for more details about the Hubbard U tests on OsX_2 monolayers, the phonon spectra, and band structures.

[31] J. Heyd, G. Scuseria, and M. Ernzerhof, Hybrid functionals based on a screened Coulomb potential, J. Chem. Phys. **118**, 8207 (2003).

[32] A. Togo and I. Tanaka, First principles phonon calculations in materials science, Scr. Mater. **108**, 1 (2015).

[33] R. D. King-smith and D. Vanderbilt, Theory of polarization of crystalline solids, Phys. Rev. B **47**, 1651 (1993).

[34] W. Yu, J. Li, T. S. Herng, Z. Wang, X. Zhao, X. Chi, W. Fu, I. Abdelwahab, J. Zhou, J. Dan, Z. Chen, Z. Chen, Z. Li, J. Lu, S. J. Pennycook, Y. P. Feng, J. Ding, and K. P. Loh, Chemically exfoliated VSe$_2$ monolayers with room-temperature ferromagnetism, Adv. Mater. **31**, 1903779 (2019).

[35] M. Bonilla, S. Kolekar, Y. Ma, H. C. Diaz, V. Kalappattil, R. Das, T. Eggers, H. R. Gutierrez, M.-H. Phan, and M. Batzill, Strong room-temperature ferromagnetism in VSe$_2$ monolayers on van der Waals substrates, Nat. Nanotechnol. **13**, 289 (2018).

[36] B. Huang, G. Clark, E. Navarro-Moratalla, D. R. Klein, R. Cheng, K. L. Seyler, D. Zhong, E. Schmidgall, M. A. McGuire, D. H. Cobden, W. Yao, D. Xiao, P. Jarillo-Herrero, and X. Xu, Layer-dependent ferromagnetism in a van der Waals crystal down to the monolayer limit, Nature (London) **546**, 270 (2017).

[37] D. S. Wang, R. Q. Wu, and A. J. Freeman, First-principles theory of surface magnetocrystalline anisotropy and the diatomic-pair model, Phys. Rev. B **47**, 14932 (1993).

[38] H. Murakawa, Y. Onose, S. Miyahara, N. Furukawa, and Y. Tokura, Ferroelectricity induced by spin-dependent metal-ligand hybridization in $Ba_2CoGe_2O_7$, Phys. Rev. Lett. **105**, 137202 (2010).

[39] F. Wang, Y. Zhou, X. Shen, S. Dong, and J. Zhang, Magnetoelectric coupling and cross control in two-dimensional ferromagnets, Phys. Rev. Appl. **20**, 064011 (2023).

[40] Y. Zhou, H. Ye, J. Zhang, and S. Dong, Double-leaf Riemann surface topological converse magnetoelectricity, Phys. Rev. B **110**, 054424 (2024).

[41] C. Jia, S. Onoda, N. Nagaosa, and J. H. Han, Bond electronic polarization induced by spin, Phys. Rev. B **74**, 224444 (2006).

[42] N. A. Benedek and C. J. Fennie, Hybrid improper ferroelectricity: A mechanism for controllable polarization-magnetization coupling, Phys. Rev. Lett. **106**, 107204 (2011).

[43] Q. Cui, Y. Zhu, J. Liang, P. Cui, and H. Yang, Spin-valley coupling in a two-dimensional VSi_2N_4 monolayer, Phys. Rev. B **103**, 085421 (2021).

[44] K. Sheng, B. Zhang, H.-K. Yuan, and Z.-Y. Wang, Strain-engineered topological phase transitions in ferrovalley 2H-$RuCl_2$ monolayer, Phys. Rev. B **105**, 195312 (2022).

[45] R. Peng, Y. Ma, X. Xu, Z. He, B. Huang, and Y. Dai, Intrinsic anomalous valley Hall effect in single-layer Nb_3I_8, Phys. Rev. B **102**, 035412 (2020).

[46] Y. Weng and S. Dong, Manipulation of $J_{eff} = 3/2$ states by tuning the tetragonal distortion, Phys. Rev. B **104**, 165150 (2021).

[47] Y. Weng, X. Li, and S. Dong, Strong tuning of magnetism and electronic structure by spin orientation, Phys. Rev. B **102**, 180401(R) (2020).